Concurrent spatial and spectral filtering by resonant nanogratings

Manoj Niraula,[1,2] Jae Woong Yoon,[1,2] and Robert Magnusson[1,*]

[1]*Department of Electrical Engineering, University of Texas at Arlington, Box 19016, Arlington, Texas 76019, USA*
[2]*These authors contributed equally to this work*
[*]*magnusson@uta.edu*

Abstract: Optical devices incorporating resonant periodic layers constitute an emerging technological area. Recent advances include spectral filters, broadband mirrors, and polarizers. Here, we demonstrate concurrent spatial and spectral filtering as a new outstanding attribute of this device class. This functionality is enabled by a unique, near-complete, reflection state that is discrete in both angular and spectral domains and realized with carefully-crafted nanogratings operating in the non-subwavelength regime. We study the pathway and inter-modal interference effects inducing this intriguing reflection state. In a proof-of-concept experiment, we obtain angular and spectral bandwidths of ~4 mrad and ~1 nm, respectively. This filter concept can be used for focus-free spectral and spatial filtering in compact holographic and interferometric optical instruments.

OCIS codes: (050.0050) Diffraction and gratings; (230.7400) Waveguides, slab; (310.6628) Subwavelength structures, nanostructures; (230.7408) Wavelength filtering devices.

References and links

1. R. Magnusson, D. Wawro, S. Zimmerman, and Y. Ding, "Resonant photonic biosensors with polarization-based multiparametric discrimination in each channel," Sensors (Basel) **11**(2), 1476–1488 (2011).
2. Z. S. Liu, S. Tibuleac, D. Shin, P. P. Young, and R. Magnusson, "High-efficiency guided-mode resonance filter," Opt. Lett. **23**(19), 1556–1558 (1998).
3. S. Peng and G. M. Morris, "Resonant scattering from two-dimensional gratings," J. Opt. Soc. Am. A **13**(5), 993–1005 (1996).
4. J. M. Foley, S. M. Young, and J. D. Phillips, "Narrowband mid-infrared transmission filtering of a single layer dielectric grating," Appl. Phys. Lett. **103**(7), 071107 (2013).
5. S. Tibuleac and R. Magnusson, "Narrow-linewidth bandpass filters with diffractive thin-film layers," Opt. Lett. **26**(9), 584–586 (2001).
6. P. Reader-Harris, A. Ricciardi, T. Krauss, and A. Di Falco, "Optical guided mode resonance filter on a flexible substrate," Opt. Express **21**(1), 1002–1007 (2013).
7. C. F. R. Mateus, M. C. Y. Huang, Y. Deng, A. R. Neureuther, and C. J. Chang-Hasnain, "Ultrabroadband mirror using low-index cladded subwavelength grating," IEEE Photonics Technol. Lett. **16**(2), 518–520 (2004).
8. C. J. Chang-Hasnain and W. Yang, "High-contrast gratings for integrated optoelectronics," Adv. Opt. Photonics **4**(3), 379–440 (2012).
9. Y. Ding and R. Magnusson, "Resonant leaky-mode spectral-band engineering and device applications," Opt. Express **12**(23), 5661–5674 (2004).
10. D. Fattal, J. Li, Z. Peng, M. Fiorentino, and R. G. Beausoleil, "Flat dielectric grating reflectors with focusing abilities," Nat. Photonics **4**(7), 466–470 (2010).
11. J. W. Yoon, K. J. Lee, W. Wu, and R. Magnusson, "Wideband omnidirectional polarization-insensitive light absorbers made with 1D silicon gratings," Adv. Opt. Mater. **2**(12), 1206–1212 (2014).
12. E. Garnett and P. Yang, "Light trapping in silicon nanowire solar cells," Nano Lett. **10**(3), 1082–1087 (2010).
13. D. C. Marinica, A. G. Borisov, and S. V. Shabanov, "Bound states in the continuum in photonics," Phys. Rev. Lett. **100**(18), 183902 (2008).
14. C. W. Hsu, B. Zhen, J. Lee, S.-L. Chua, S. G. Johnson, J. D. Joannopoulos, and M. Soljačić, "Observation of trapped light within the radiation continuum," Nature **499**(7457), 188–191 (2013).
15. J. W. Yoon, M. J. Jung, S. H. Song, and R. Magnusson, "Analytic theory of the resonance properties of metallic nanoslit arrays," IEEE J. Quantum Electron. **48**(7), 852–861 (2012).
16. L. Mashev and E. Popov, "Zero order anomaly of dielectric coated gratings," Opt. Commun. **55**(6), 377–380 (1985).
17. M. Flury, A. V. Tishchenko, and O. Parriaux, "The leaky mode resonance condition ensures 100% diffraction efficiency of mirror-based resonant gratings," J. Lightwave Technol. **25**(7), 1870–1878 (2007).

#240080 Received 30 Apr 2015; revised 25 Aug 2015; accepted 26 Aug 2015; published 28 Aug 2015

18. N. Vermeulen, P. Wasylczyk, S. Tonchev, P. Muys, H. Ottevaere, O. Parriaux, and H. Thienpont, “Low-loss wavelength tuning of a mid-infrared Cr^{2+}:ZnSe laser using a littrow-mounted resonant diffraction grating,” Laser Phys. Lett. **8**(8), 606-612 (2011).
19. J. Kennedy and R. Eberhart, “Particle swarm optimization,” Proceedings of the IEEE International Conference on Neural Networks **4**, 1942–1948 (1995).
20. M. G. Moharam, D. A. Pommet, E. B. Grann, and T. K. Gaylord, “Stable implementation of the rigorous coupled-wave analysis for surface-relief gratings: enhanced transmittance matrix approach,” J. Opt. Soc. Am. A **12**(5), 1077–1086 (1995).
21. R. Magnusson, “Flat-top resonant reflectors with sharply delimited angular spectra: an application of the Rayleigh anomaly,” Opt. Lett. **38**(6), 989–991 (2013).
22. D. Rosenblatt, A. Sharon, and A. A. Friesem, “Resonant grating waveguide structures,” IEEE J. Quantum Electron. **33**(11), 2038–2059 (1997).
23. J. Yoon, K. H. Seol, S. H. Song, and R. Magnusson, “Critical coupling in dissipative surface-plasmon resonators with multiple ports,” Opt. Express **18**(25), 25702–25711 (2010).

---

1. Introduction

Subwavelength periodic structures enable versatile applications including label-free optical biosensors [1], high-performance optical filters [2–6], broadband reflectors [7–9], beam-transforming meta-surfaces [10], absorbers [11,12], and high-Q optical resonators [13,14]. In the subwavelength regime with only zero-order external propagating waves, coupling of an input excitation wave with a resonant leaky mode can be modeled as a generic two-port resonance system. In lossless systems, the attendant resonant reflectance is unity regardless of the details of the particular coupling configuration [15]. Therefore, the resonance spectra in reflection and transmission form angular continua on characteristic dispersion bands in the angle-wavelength space [9,16]. In contrast, here we show that non-subwavelength nanogratings with multiple propagative diffraction channels enable an angularly discrete resonance response. Previously it was shown that high first-order diffraction efficiency can be achieved with non-subwavelength resonant gratings. In particular, Parriaux and associates reported near-total first-order reflection from mirror-based waveguide-grating structures [17,18]. There are no prior reports on discrete angular resonance states as provided in this paper.

2. Proposed device

Our device concept is illustrated in Fig. 1(a). The reflection is confined to a narrow, collimated spectral channel even under wideband diverging or converging incident light. Obtaining efficient zero-order reflection in the non-subwavelength regime involves simultaneous suppression of all other propagating orders. We accomplish this by parametric optimization applying the particle-swarm optimization (PSO) method [19]. We use a rigorous coupled-wave analysis (RCWA) [20] algorithm as the forward computational kernel in our PSO code. We model a partially-etched TiO_2 waveguide grating on a glass substrate as shown in Fig. 1(a). The angle-dependent zero-order reflectance (R_0) spectrum under transverse-electric (TE) polarized light incidence in Fig. 1(b) shows the unique discrete angular/spectral reflection state at $\lambda = 852$ nm under normal incidence ($\theta = 0$). The reflection peak has 99.8% efficiency and full-width-at-half-maximum (FWHM) bandwidths of $\Delta\lambda = 0.6$ nm in wavelength and $\Delta\theta = 0.12°$ in angle. In the 1550~1700 nm spectral band, this device transits to the subwavelength regime where different functionality prevails. Figure 1(c) shows the corresponding spectrum; it is clearly completely different than the spectrum in Fig. 1(b). The chief objective of this Letter is to explain this dramatic difference and provide experimental verification of the predicted discrete spectra.

The inset in Fig. 2(a) shows the electric field distribution at the reflection peak center and the propagating waves associated with the device. The resonance is induced by a standing TE_0 guided mode coupling to four external waves R_0, T_0, and $T_{\pm 1}$. The spectra in Figs. 2(a) and 2(b) show high-efficiency reflectance R_0 even with multiple simultaneous propagating waves that generally reduce the power available to it. The non-resonant background shows weak zero-order intensities R_0 and T_0 with most of the incident energy coupling to the two transmitted first-order substrate waves $T_{\pm 1}$. We remark that this effect is not associated with

#240080 Received 30 Apr 2015; revised 25 Aug 2015; accepted 26 Aug 2015; published 28 Aug 2015

any Rayleigh-type power exchange [21]. The resonant excitation of the standing TE_0 guided mode at $\lambda = 852$ nm and $\theta = 0$ exchanges the dominant diffraction channel from $T_{\pm 1}$ to R_0 while T_0 remains persistently low. This new, intriguing power transfer mechanism requires detailed analysis.

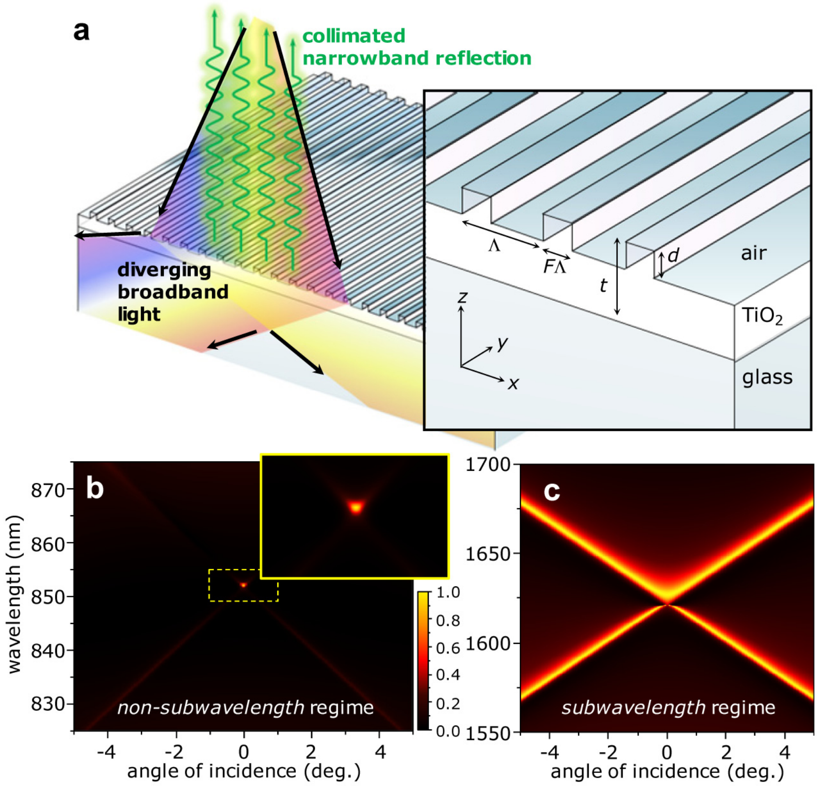

Fig. 1. Theoretical reflectance showing spatial/spectral delta function characteristics. (a) Device schematic. The geometry is defined by the grating period Λ; fill factor F; total film thickness t and grating depth d. Refractive indices are $n_F = 2.52$ for the TiO_2 film, $n_S = 1.54$ for the glass substrate, and $n_C = 1.0$ for air. (b) Computed angle-dependent zero-order reflectance (R_0) spectrum of an optimized device under TE-polarized light incidence (electric field vector along y). The optimized parameters are $\Lambda = 696$ nm, $F = 0.33$, $t = 788$ nm, and $d = 210$ nm. (c) Angle-dependent R_0 spectrum of the same device in the subwavelength regime in the 1550~1700 nm wavelength region.

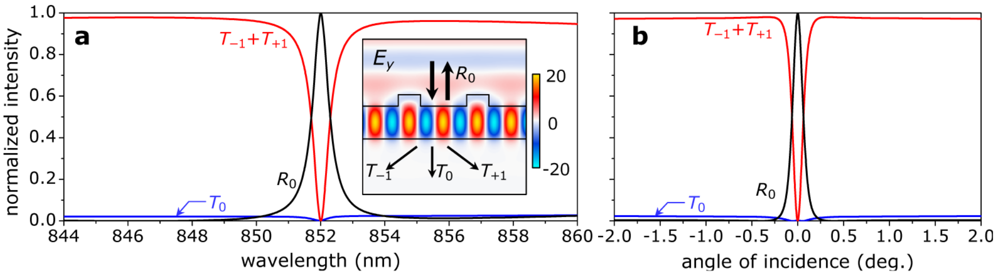

Fig. 2. Diffraction efficiency pertinent to the device in Fig. 1. (a) Spectra of all propagating orders under normal incidence. (b) Angular spectra of all propagating orders at wavelength λ = 852 nm. Inset in (a) shows the localized electric field amplitude distribution at the reflection-peak wavelength. The field amplitude is normalized by the incident field amplitude. The y-axis in (a) and (b) are identical.

3. Pathway and intermodal effects analysis

The discrete angular/spectral reflection state observed in Fig. 2 can be explained by invoking two distinct interference mechanisms. First, interference between resonant and non-resonant diffraction pathways plays an important role. Figure 3(a) illustrates the two different diffraction pathways. The incident wave couples to four propagating diffraction orders. These are the zero-order reflected wave, zero-order transmitted wave, and two first-order transmitted waves. The second-order diffracted wave in the TiO_2 layer is totally reflected at the bottom TiO_2-glass interface and drives a TE_0-type mode yielding a guided-mode resonance mechanism [2]. Therefore, re-radiation of the mode to each outgoing diffraction order constitutes the resonant pathway. As indicated in Fig. 3(a), $\rho_0^{(R)}$, $\tau_0^{(R)}$, and $\tau_{\pm 1}^{(R)}$ refer to the *resonant* zero-order reflection, zero-order transmission, and first-order transmission amplitudes, respectively. Consequently, the non-resonant pathway corresponds to all other diffraction pathways which do not involve the second-order diffraction in the TiO_2 layer. The *non-resonant* diffraction amplitudes are thus denoted by $\rho_0^{(N)}$, $\tau_0^{(N)}$, and $\tau_{\pm 1}^{(N)}$. Analogous interference picture applies to reflection resonances in the zero-order regime [22]. The intensity of the outgoing diffraction orders is expressed by a superposition such that $R_0 = |\rho_0^{(N)} + \rho_0^{(R)}|^2$, $T_0 = |\tau_0^{(N)} + \tau_0^{(R)}|^2$, and $T_{\pm 1} = |\tau_{\pm 1}^{(N)} + \tau_{\pm 1}^{(R)}|^2$. The non-resonant amplitudes contribute the sideband intensity in the spectra. In the spectra in Figs. 2(a) and 2(b), we see that $\rho_0^{(N)} \approx 0$, $\tau_0^{(N)} \approx 0$, and $\tau_0^{(R)} \approx 0$ such that $R_0 \approx |\rho_0^{(R)}|^2$ and $T_0 \approx 0$. At the reflection peak center at $\lambda = 852$ nm and $\theta = 0$ in Figs. 2(a) and 2(b) we see that $T_{\pm 1} \approx 0$ implying a nearly complete destructive interference between $\tau_{\pm 1}^{(N)}$ and $\tau_{\pm 1}^{(R)}$, meaning that there is a π phase difference between the two pathways with equal amplitudes, i.e., $\tau_{\pm 1}^{(N)} \approx -\tau_{\pm 1}^{(R)}$. By energy conservation this implies $R_0 \approx |\rho_0^{(R)}|^2 \approx 1$. The optimized structure is designed so that complete destructive pathway interference occurs in the first-order transmission channels at $\theta = 0$.

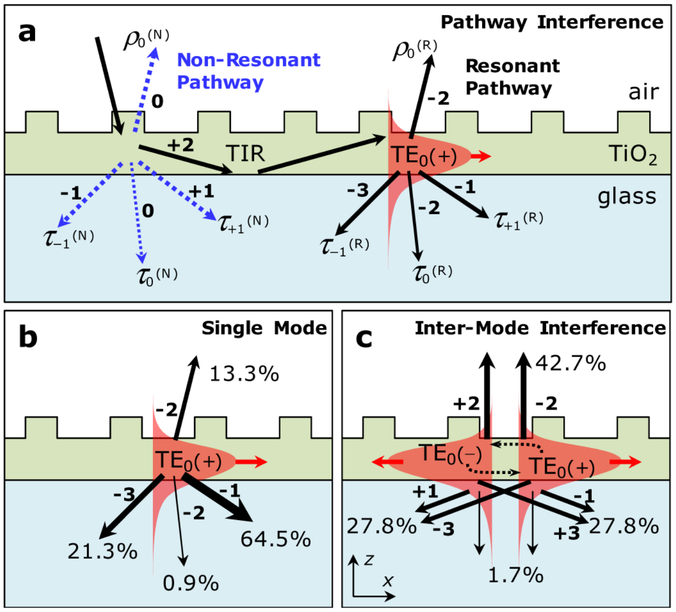

Fig. 3. Interference effects associated with the discrete angular/spectral reflection. (a) Radiation pathways hypothesized to explain the observed spectra. The non-resonant pathway is formed by direct diffraction of the incident light. The resonant pathway is defined by leakage radiation stimulated by a TE_0 mode coupling through second-order diffraction. Integer numbers label dominant coupling diffraction orders for waves indicated by the arrows. (b) Leakage radiation probabilities pertaining to a traveling TE_0 mode at $\lambda = 848$ nm and $\theta = 0.565°$. (c) Leakage radiation probabilities associated with counter-propagating leaky modes at $\lambda = 852$ nm and $\theta = 0$.

#240080 Received 30 Apr 2015; revised 25 Aug 2015; accepted 26 Aug 2015; published 28 Aug 2015

Under off-normal incidence, the destructive pathway interference in the first-order transmission becomes incomplete due to asymmetry in $\tau_{+1}^{(R)}$ and $\tau_{-1}^{(R)}$. In Fig. 3(b), we indicate the leakage radiation probabilities associated with a TE_0 guided mode resonating at λ = 848 nm at a small off-normal angle ($\theta = 0.565°$). The leakage radiation probabilities are calculated by the absorbance analysis method proposed in [23] with following equation for peak absorbance

$$A_n = 4\eta_{abs}\eta_n, \tag{1}$$

where A_n is peak absorbance under wave incidence at radiation channel n, η_{abs} is absorption probability, and η_n is radiation probability of the resonant mode to radiation channel n. Equation (1) can be used for inferring radiation probabilities even in lossless cases with $A_n = 0$ by taking the asymptotic limit

$$\eta_n = \lim_{k \to 0} \frac{A_n}{\sum_m A_m}, \tag{2}$$

where the index m in the summation runs over all the available radiation channels and k is the extinction coefficient of the material forming the resonator under consideration. For the single TE_0 mode in Fig. 3(b), the radiation probabilities into $\tau_{+1}^{(R)}$ and $\tau_{-1}^{(R)}$ are 64.5% and 21.3%, respectively, denoting substantial asymmetry. This is a natural consequence of the difference in the coupling orders as $\tau_{+1}^{(R)}$ is emitted as first-order diffraction of the driving mode whereas $\tau_{-1}^{(R)}$ is generated by a third-order diffraction process. In contrast, the non-resonant amplitudes are approximately symmetric, i.e., $\tau_{+1}^{(N)} \approx \tau_{-1}^{(N)}$, because they both couple through a first-order process at small angle of incidence. Therefore, for $\theta \neq 0$, pathway interference in T_{+1} and T_{-1} cannot be identically destructive, resulting in sizable intensity in the first-order transmission channels and a weaker R_0 at resonance.

The enhancement of R_0 on resonance at $\theta = 0$ involves interference between secondary waves radiated by counter-propagating leaky modes. In Fig. 3(c), we show the radiation probabilities and coupling orders for the standing TE_0 mode at λ = 852 nm and $\theta = 0$ corresponding to the resonance center of the discrete angular/spectral reflection state. We confirm that the radiation probability towards zero-order reflection is remarkably enhanced to 42.7% for the standing-mode case relative to 13.3% for the traveling-mode case in Fig. 3(b). In contrast, as noted in Fig. 3(c), the net radiation probability to the first-order transmission channels is substantially reduced. In Fig. 3(c), the $TE_0(+)$ mode traveling in the $+x$ direction couples to the T_{+1} channel through first-order diffraction while the $TE_0(-)$ mode traveling along $-x$ contributes to this channel by third-order diffraction. We calculate the phase difference between these two contributions finding ~1.09π. The close-to-π phase difference provides destructive interference between the two constitutive components generated by the modes running along $\pm x$. This reduces the amplitude of $\tau_{\pm 1}^{(R)}$ sufficiently to enable their final extinction by interference with $\tau_{\pm 1}^{(N)}$.

4. Experimental results

Proof-of-concept experiments verify the proposed concept. We fabricate devices using sputtered TiO_2 films on microscope slides applying UV-laser interference lithography and reactive-ion etching. Shown in Figs. 4(a) and 4(b) are scanning electron micrographs of the fabricated device. From these micrographs, the measured device parameters are period $\Lambda = 753$ nm, fill factor $F = 0.25$, TiO_2-film thickness $t = 602$ nm and grating depth $d = 210$ nm. The measured R_0 spectrum is shown in Fig. 4(c). We clearly observe a discrete reflection peak at λ = 812 nm and $\theta = 0$. The RCWA calculation assuming the device structure indicated by the red-dashed lines in Fig. 4(b) shows excellent *quantitative* agreement with the experimental results as indicated in Figs. 4(d) and 4(e). In the experiment, the resonance peak attains 80.1% efficiency and FWHM bandwidth of 1.42 nm in wavelength and 0.24° in angle.

#240080 Received 30 Apr 2015; revised 25 Aug 2015; accepted 26 Aug 2015; published 28 Aug 2015

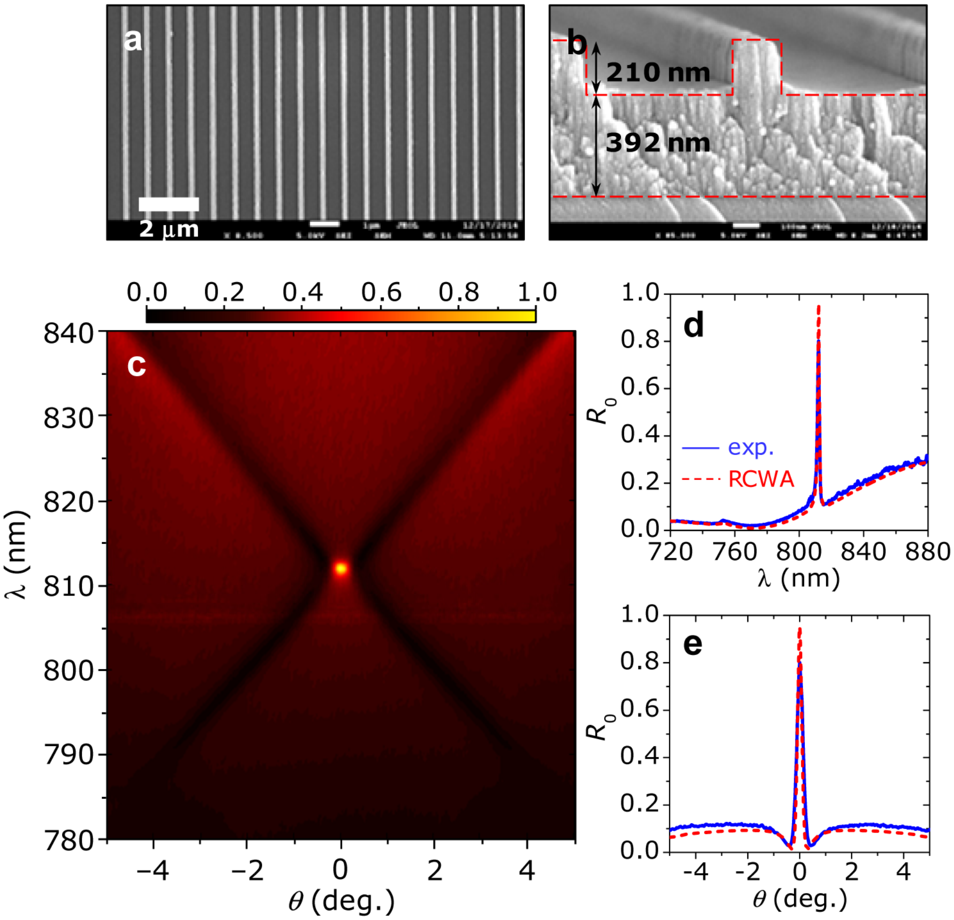

Fig. 4. Experimental demonstration of a discrete angular and spectral reflector. (a) Top-view and (b) cross-sectional scanning electron micrographs of the fabricated device. Red-dashed lines in (b) indicate the structure used in the numerical calculation (RCWA) for comparison. (c) Measured angle-dependent R_0 spectrum. (d) Measured spectra and comparison with numerical calculation under normal incidence. (e) Angular spectrum at wavelength λ = 812 nm.

5. Spatial-filtering application

An interesting potential use of the narrow angular selectivity is focus-free spatial filtering. In many applications, spatial filters are necessary to eliminate spatial noise associated with random laser fluctuation and scattering. Figure 5(a) shows conventional spatial filtering applying a pair of lenses and a pinhole. In this arrangement, high-accuracy optical alignment is required. Moreover, high-power applications are limited by potential pinhole thermal failure. Our device avoids these limitations owing to its focus-free spatial filtering property as illustrated in Fig. 5(b). In this example, the spatial filter rejects high-frequency noise components without a focusing lens and pinhole.

We numerically demonstrate example performance of a focus-free spatial filter in this class. We design an ultra-sharp angular reflector with peak reflectance ~99.9% at wavelength λ = 874.069 nm and bandwidths of $\Delta\theta = 0.005°$ and Δλ = 23 pm as shown in Fig. 5(c). This angular bandwidth corresponds to a conventional spatial filter using a pinhole with a 1.7-μm diameter and an objective lens with focal length of 10 mm. The top TiO_2 grating of this design is identical to the design in Fig. 1 but the new design has a thicker TiO_2 sublayer. The filtering performance of this element is presented in Fig. 5(d). We assume a 16-mm-wide TE-

#240080 Received 30 Apr 2015; revised 25 Aug 2015; accepted 26 Aug 2015; published 28 Aug 2015

polarized super-Gaussian beam carrying computer-generated pseudo-random noise as input light. The electric field of the beam is given by

$$E_{\text{in}}(x) = E_0 \left[1 + a f(x)\right]^{1/2} \exp\left[-\frac{1}{2}\left(\frac{x}{w}\right)^4\right], \tag{3}$$

where a is a normalized amplitude of the computer-generated pseudo-random function $f(x)$ with [–1/2, 1/2] range and w is the beam width. The filtered output beam intensity is calculated by using the Fourier-decomposition method with the equations

$$\varepsilon_{\text{in}}(\theta) = \int_{-\infty}^{+\infty} E_{\text{in}}(x) e^{-i2\pi x\cos\theta/\lambda} dx, \tag{4}$$

$$E_{\text{out}}(x) = \frac{1}{\lambda} \int_{-\pi/2}^{+\pi/2} \rho_0(\theta)\varepsilon_{\text{in}}(\theta) e^{i2\pi x\cos\theta/\lambda} \cos\theta d\theta, \tag{5}$$

where λ is wavelength and $\rho_0(\theta)$ is the complex reflection coefficient of the discrete angular reflector. This formalism is valid for the far-field filtering property where evanescent components in the incident beam transfer no signal to the output beam. The intensity profiles in Fig. 5(d) are calculated by taking the absolute square of the electric field amplitudes, i.e., $|E_{\text{in}}|^2$ and $|E_{\text{out}}|^2$. The input beam parameters used in Fig. 5(d) are $a = 0.5$ and $w = 10$ mm. We find that the noise in the filtered output beam is reduced by a factor of ~17. The filtered output profile maintains the flat-top property of the input super-Gaussian beam in contrast to the sharp-top Airy disk profile characteristics of conventional spatial filters.

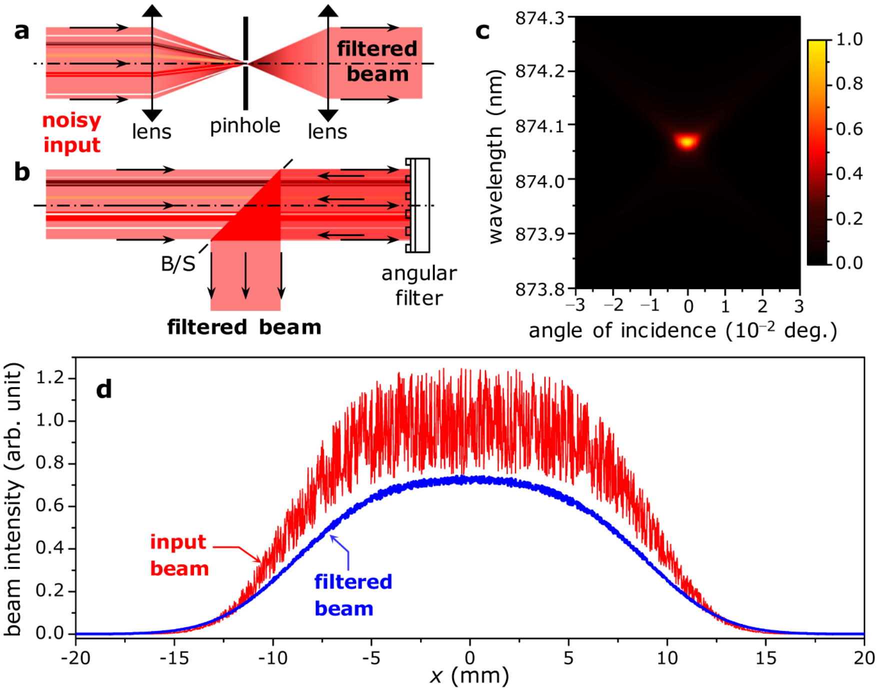

Fig. 5. Spatial filtering with a discrete angular reflector element. (a) Conventional spatial filter using a pinhole/lens pair. (b) Proposed spatial/spectral filter fashioned with a resonant nanograting. (c) Reflectance spectrum of the spatial/spectral filter. The device parameters are $\Lambda = 696$ nm, $F = 0.33$, $t = 2210$ nm, and $d = 210$ nm. (d) Theoretical performance of the spatial filter with an input super-Gaussian laser beam with FWHM width of 16 mm carrying computer-generated pseudo-random noise.

#240080 Received 30 Apr 2015; revised 25 Aug 2015; accepted 26 Aug 2015; published 28 Aug 2015

6. Conclusions

To conclude, we provide a new spatial/spectral filter concept based on guided-mode resonance effects in the non-subwavelength regime. We show that complex inter-modal and pathway interference processes enable these unique angular and spectral properties that are not feasible in the subwavelength regime. The experimental results show excellent quantitative agreement with theoretical predictions. We numerically demonstrate focus-free spatial filtering with the proposed device concept. We remark that the pathway and inter-modal interference effects invoked in the physical explanation of the device operation represent general aspects of guided-mode resonance phenomena in the non-subwavelength regime. Therefore, we expect high-efficiency spatial/spectral selectivity to be feasible in other diffraction channels including in zero-order transmission T_0. Developing such elements in connection with appropriate tuning methods may enable innovative solutions for directional and spectral beam management in solid-state light emitters without bulky external components.

Acknowledgments

The research leading to these results was supported in part by the Texas Instruments Distinguished University Chair in Nanoelectronics endowment.